

Perturbative Renormalisation Group Improved Black Hole Solution and its Quasinormal Modes

Rupam Jyoti Borah^{*} and Umananda Dev Goswami[†]

Department of Physics, Dibrugarh University, Dibrugarh 786004, Assam, India

In this work, we construct a perturbative black hole (BH) solution motivated by renormalization group (RG) improvement and investigate the quasinormal modes (QNMs) of the BH under scalar field perturbations in both Schwarzschild-de Sitter (SdS) and Schwarzschild-anti-de Sitter (SAdS) backgrounds. To compute the QNMs in the SdS spacetime, we employ the 6th-order Padé-averaged WKB approximation method, while for the SAdS background we utilize the direct shooting method. We examine the dependence of the QNM frequencies on the free parameter of the solution. Furthermore, we analyze the time evolution of a scalar field perturbation around the BH and present the corresponding time-domain profiles. The QNMs are also extracted from the time-domain data using the matrix pencil method. Using the extracted QNM frequencies, we reconstruct the waveform and compare it with the original time-domain profile, finding good agreement between the two. The QNM frequencies obtained from the 6th-order Padé-averaged WKB method and the time-domain analysis in the SdS background, as well as those obtained from the direct shooting method and time-domain analysis in the SAdS spacetime, show very good consistency.

Keywords: Renormalisation group; Quantum gravity; Quasinormal modes; Black holes.

I. INTRODUCTION

General Relativity (GR) has remained as the most successful classical description of gravity since its formulation. Over the years, it has undergone rigorous experimental tests with astrophysical observations for its predictions, and has been consistently verified to remarkable accuracy. Two major achievements in recent times further highlight its success: the direct detection of gravitational waves (GWs) by the LIGO collaboration [1–5], and the first-ever and subsequent images of BHs captured by the Event Horizon Telescope (EHT) collaboration [6–11]. Despite these successes, GR has shown some limitations. For instance, it does not provide a satisfactory explanation for the observed accelerated expansion of the Universe (the dark energy problem), and it can't fully account for the missing mass problem, commonly called the dark matter problem [12–15]. Moreover, when gravity is treated as a fundamental interaction at extremely high energy scales, where quantum effects are expected to play a crucial role, GR becomes inadequate. Thus, GR fails to explain the behaviour of gravity at very high energy scales where Quantum Gravity (QG) effects become dominant. While the Standard Model (SM) of particle physics successfully describes the strong, electromagnetic, and weak interactions within the framework of Quantum Field Theory (QFT), it fails to include gravity because GR, in its conventional form, is not renormalizable. The goal to unify GR with the SM remains one of the central challenges in theoretical physics. In pursuit of this goal, several candidate theories of QG have been proposed to describe gravity at very high energy scales [16–21]. Loop Quantum Gravity (LQG) [22–25] and String Theory [26–30] are among the most extensively studied approaches. String Theory aims to provide a unified description of all four fundamental interactions within a single theoretical framework, and it predicts the existence of the graviton as the mediator particle of gravitational interaction. In contrast, LQG focuses specifically on the quantization of the gravitational field; it suggests that spacetime possesses a discrete structure composed of fundamental quantum units.

Although LQG and String Theory are among the most extensively studied approaches to QG, their predictions have not yet been tested experimentally. The main difficulty lies in the extremely high energy scales at which their distinctive quantum gravitational effects are expected to appear. These energies are far beyond the capabilities of present day experimental facilities, making direct verification of these theories currently impractical. Due to these limitations, other theoretical approaches have been explored to investigate possible QG effects within accessible energy scales. One such approach is the framework of Effective Field Theory (EFT). In this perspective, GR is treated as an effective theory that remains valid up to a certain cutoff scale. This allows quantum corrections to be systematically incorporated into the theory, while ensuring that the theory reduces to classical GR in the low-energy regime. Several works have been successfully done by considering gravity as an EFT [31–36]. It is worth noting that EFT typically predicts only small quantum corrections at low energies. However, these corrections can become important in regions of extreme gravity, such as near the event horizon of a BH or in the early Universe. Therefore, BHs provide one of the most promising environments for probing QG effects within our current theoretical and observational reach. Motivated by this, many studies have investigated BH properties within the EFT framework [37–45].

Apart from the approaches discussed above, another promising framework for QG is the asymptotically safe gravity [46–51]. Within the framework of the asymptotic safety scenario of QG, the primary objective is to establish a consistent and predictive

* Email: rupamjyotiborah856@gmail.com

† Email: umananda@dibru.ac.in

ultraviolet (UV) completeness of gravity. The central idea is that gravitational interactions may approach a non-Gaussian fixed point under the renormalization group (RG) flow at high energy scales. If such a fixed point exists, the theory remains finite and well defined in the UV regime. To investigate this possibility, the asymptotic safety approach employs a covariant formulation of the Wilsonian renormalization group [52–54]. Within this framework, Newton’s gravitational constant G and the cosmological constant Λ are treated as scale dependent quantities that acquire explicit spacetime dependence, denoted by $G(x)$ and $\Lambda(x)$, where $x \equiv x^\mu$. The introduction of the effective average action and its associated functional RG equation provides a concrete realization of this program [55, 56]. In this framework, a scale dependent effective action is constructed, which implements a Wilsonian RG flow on the space of all diffeomorphism invariant functionals of the metric. The UV consistency of the theory is then governed by the existence of a non-Gaussian fixed point of the RG flow, rather than by a direct quantization of classical GR. Such effective average action is closely related to the standard effective action and defines a family of scale dependent EFTs labeled by a particular momentum (energy) scale. For a physical system characterized by a single momentum scale, quantum corrections can be incorporated by evaluating the effective action at the corresponding scale, thereby implementing renormalization group improvement. This approach thus provides a systematic framework for encoding QG effects through scale-dependent couplings. Motivated by these developments, Refs. [57, 58] constructed an RG improved effective gravitational action and the corresponding modified field equations. In this framework, the running of the gravitational couplings obtained from the RG flow is incorporated into the classical action, leading to scale dependent corrections to Einstein’s field equations. The resulting field equations can be solved perturbatively by expanding around a classical GR background in low-energy limits. The parameters of the perturbative expansion quantify the deviation of the running couplings from their classical constant values. Such solutions capture the leading QG corrections and provide small but systematic modifications to BH spacetimes. The imprints of these corrections may be reflected in various BH observables, including quasinormal modes (QNMs), BH shadows, and other phenomena associated with strong gravitational fields [59–65].

QNMs represent the characteristic damped oscillations of BHs and provide direct information about their fundamental parameters. The associated complex frequencies depend on intrinsic properties such as the mass, angular momentum, and charge of the BHs. Any modification to the underlying spacetime geometry, particularly those arising from QG effects, can induce measurable shifts in these frequencies. In several QG frameworks, including LQG and String Theory, corrections to a classical BH metric naturally lead to deviations in the QNM spectrum. Moreover, within the context of the AdS/CFT correspondence, QNMs in asymptotically anti-de Sitter spacetimes are related to the relaxation dynamics of strongly coupled QFTs [66, 67]. This correspondence highlights the broader significance of QNMs, suggesting that their study can shed light on the quantum aspects of gravitational systems. For these reasons, QNMs serve as powerful probes of possible QG imprints in BH spacetimes and have been extensively investigated across a wide range of gravitational theories in recent years [68–77].

Motivated by the above considerations, in this study, we construct a perturbative BH solution from the RG improved field equations presented in Refs. [57, 58] and investigate the QNMs of the corresponding BH solution.

The rest of the paper is organized as follows. In Section II, we briefly review the RG improved action and the associated RG improved field equations. In Section III, we derive a perturbative BH solution that captures the QG effects arising from RG improvement in the low-energy regime. In Section IV, we analyze the QNMs of the BH in both Schwarzschild-de Sitter (SdS) and Schwarzschild-Anti-de Sitter (SAdS) spacetimes for a scalar field perturbation. In Section V, we study the time-domain profile of a scalar field perturbation around the BH and extract the QNMs from the corresponding time evolution. Finally, in Section VI, we summarize our results and present our conclusions.

II. RENORMALISATION GROUP IMPROVED FIELD EQUATIONS

As stated earlier, the RG improvement provides a systematic way to incorporate scale dependent quantum corrections into classical gravitational dynamics. The RG improved field equations considered in this work admit two equivalent derivations in the literature. In Ref. [57], the field equations were obtained directly by imposing covariance and consistency conditions. Subsequently, in Ref. [58], the authors constructed an effective action whose variation with respect to the metric reproduces the field equations derived in Ref. [57]. In this section, we first outline the key assumptions and essential steps underlying the derivation of the RG-improved field equations in Ref. [57]. We then summarize the construction of the corresponding effective action following the Lagrangian framework developed in Ref. [58].

In Ref. [57], the authors considered a spacetime dependent cosmological constant $\Lambda(x)$ and Newton’s constant $G(x)$, so Einstein field equations with an energy-momentum tensor $T_{\mu\nu}$ can be written as

$$G_{\mu\nu} = -\Lambda(x)g_{\mu\nu} + 8\pi G(x)T_{\mu\nu} \quad (1)$$

Now, the Bianchi identities suggest the consistency condition for these equations as

$$8\pi(GT_{\mu\nu})^{;\mu} = \Lambda_{;\nu}, \quad (2)$$

where semicolon (;) denotes the usual covariant differentiation. However, in the presence of spacetime dependent gravitational couplings $G(x)$ and $\Lambda(x)$, the consistency condition Eq. (2) is no longer identically satisfied. Moreover, in the vacuum, Eq. (2)

implies that the cosmological constant must be a constant. It therefore becomes evident that the Bianchi identities, $G_{\mu\nu}{}^{;\mu} = 0$, cannot be satisfied without introducing additional contributions. Consequently, the field equations must be supplemented by extra covariant derivative terms involving the spacetime dependent couplings $G(x)$ and $\Lambda(x)$, as well as terms involving the energy-momentum tensor $T_{\mu\nu}$. To proceed further in direction with convenience, $G(x)$ and $\Lambda(x)$ can be parametrized as

$$G(x) = \bar{G}e^\chi, \quad \Lambda = \bar{\Lambda}e^\xi, \quad (3)$$

where $\chi(x)$ and $\xi(x)$ are prescribed spacetime dependent functions whose behaviour is fixed by the RG flow, and consequently, they do not satisfy any equations of motion. \bar{G} and $\bar{\Lambda}$ are arbitrary reference values. This parametrization, given in Eq. (3), imposes the restriction that the spacetime dependent couplings $G(x)$ and $\Lambda(x)$ are not allowed to change sign along the RG flow. A further requirement is that all additional kinetic terms vanish in the limit where $G(x)$ and $\Lambda(x)$ are constant, thereby ensuring the recovery of the classical Einstein field equations. With this parametrization and the consideration that the kinetic terms should have minimum one derivative of $\chi(x)$ and $\xi(x)$, the Einstein field equations with all possible such kinetic terms can be written as

$$G_{\mu\nu} = -\Lambda g_{\mu\nu} + \vartheta_{\mu\nu} + \tilde{\vartheta}_{\mu\nu} + \mathcal{F}(\xi_{;\mu}\chi_{;\nu} + \xi_{;\nu}\chi_{;\mu}) + \mathcal{H}g_{\mu\nu}\xi^{;\rho}\chi_{;\rho} + 8\pi GT_{\mu\nu}, \quad (4)$$

where $g_{\mu\nu}$ is the metric tensor and

$$\vartheta_{\mu\nu} = \mathcal{A}\xi_{;\mu}\xi_{;\nu} + \mathcal{B}g_{\mu\nu}\xi^{;\rho}\xi_{;\rho} + \mathcal{C}\xi_{;\mu;\nu} + \mathcal{E}g_{\mu\nu}\square\xi \quad (5)$$

is the energy-momentum tensor containing all possible kinetic terms of $\xi(x)$ and

$$\tilde{\vartheta}_{\mu\nu} = \tilde{\mathcal{A}}\chi_{;\mu}\chi_{;\nu} + \tilde{\mathcal{B}}g_{\mu\nu}\chi^{;\rho}\chi_{;\rho} + \tilde{\mathcal{C}}\chi_{;\mu;\nu} + \tilde{\mathcal{E}}g_{\mu\nu}\square\chi \quad (6)$$

is the energy-momentum tensor containing all possible kinetic terms of $\chi(x)$. All coefficients \mathcal{A} , \mathcal{B} , \mathcal{C} , \mathcal{E} , $\tilde{\mathcal{A}}$, $\tilde{\mathcal{B}}$, $\tilde{\mathcal{C}}$, $\tilde{\mathcal{E}}$, as well as \mathcal{F} and \mathcal{H} , are functions of $\xi(x)$ and $\chi(x)$. After a few substitutions and simplifications, the Bianchi identities that arise from Eq. (4) are

$$\vartheta^{;\mu}_{\mu\nu} + \tilde{\vartheta}^{;\mu}_{\mu\nu} - \bar{\Lambda}e^\xi\xi_{;\nu} + \mathcal{F}'\xi^{;\mu}\xi_{;\mu}\chi_{;\nu} + \dot{\mathcal{F}}\chi^{;\mu}\chi_{;\mu}\xi_{;\nu} + (\mathcal{F}' + \mathcal{H}')\xi^{;\mu}\chi_{;\mu}\xi_{;\nu} + (\dot{\mathcal{F}} + \dot{\mathcal{H}})\xi^{;\mu}\chi_{;\mu}\chi_{;\nu} + \mathcal{F}\square\xi\chi_{;\nu} + \mathcal{F}\square\chi\xi_{;\nu} + (\mathcal{F} + \mathcal{H})\xi^{;\mu}\chi_{;\mu;\nu} + (\mathcal{F} + \mathcal{H})\chi^{;\mu}\xi_{;\mu;\nu} + 8\pi\bar{G}e^\chi(T_{\mu\nu}{}^{;\mu} + T_{\mu\nu}\chi^{;\mu}) = 0, \quad (7)$$

where the prime and dot denote differentiation with respect to $\xi(x)$ and $\chi(x)$, respectively. The coefficients \mathcal{A} , \mathcal{B} , \mathcal{C} , \mathcal{E} , $\tilde{\mathcal{A}}$, $\tilde{\mathcal{B}}$, $\tilde{\mathcal{C}}$, $\tilde{\mathcal{E}}$ can be determine from the Bianchi relation (7) as

$$\mathcal{A} = -\frac{1}{2}, \quad \mathcal{B} = -\frac{1}{4}, \quad \mathcal{C} = 1, \quad \mathcal{E} = -1, \quad \tilde{\mathcal{A}} = \tilde{\mathcal{B}} = \tilde{\mathcal{C}} = \tilde{\mathcal{E}} = \mathcal{H} = \mathcal{F} = 0. \quad (8)$$

Thus, Eq. (4) finally becomes:

$$G_{\mu\nu} = 8\pi GT_{\mu\nu} - \bar{\Lambda}e^\xi g_{\mu\nu} - \frac{1}{2}\xi_{;\mu}\xi_{;\nu} - \frac{1}{4}g_{\mu\nu}\xi^{;\rho}\xi_{;\rho} + \xi_{;\mu;\nu} - g_{\mu\nu}\square\xi \quad (9)$$

with conservation equation:

$$(GT_{\mu\nu})^{;\mu} + G\left(T_{\mu\nu} - \frac{1}{2}Tg_{\mu\nu}\right)\xi^{;\mu} = 0. \quad (10)$$

Motivated by the results of Ref. [57], the authors of Ref. [58] developed a Lagrangian framework for the field equations given in Eq. (9). In fact, they constructed an effective action by treating the field equations as input, such that variation of this action with respect to the metric tensor reproduces Eq. (9). The steps involved in the construction of the action are as follows. As the field equations contain the Einstein tensor, which is not coupled to any additional fields, therefore, the Ricci scalar must be included in the action. Furthermore, the last two terms, $\xi_{;\mu;\nu}$ and $g_{\mu\nu}\square\xi$, appearing in Eq. (9), naturally arise in scalar-tensor theories due to the nonminimal coupling between the scalar field and gravity. These considerations indicate that the scalar field $\xi(x)$ must be coupled nonminimally to the Ricci tensor, while preserving the linear appearance of the Einstein tensor in the equations of motion. Thus, the Lagrangian should have a dilatonic type coupling and can be written in the following form:

$$\mathcal{L} \sim F(\xi)[R + \dots], \quad (11)$$

where $F(\xi)$ is a function of the scalar field $\xi(x)$. The 3rd and 4th terms in Eq. (9) i.e. $\frac{1}{2}\xi_{;\mu}\xi_{;\nu}$ and $\frac{1}{4}g_{\mu\nu}\xi^{;\rho}\xi_{;\rho}$ can be obtained from a kinetic term of field $\xi(x)$ appearing in the Lagrangian of the form:

$$\mathcal{L} \sim \omega(\xi_{;\mu})^2, \quad (12)$$

where ω is a coupling paramter. Further, the 1st term $8\pi GT_{\mu\nu}$ emerges due to a nonminimal coupling of matter Lagrangian \mathcal{L}_m with the Newton's constant and the 2nd term $\bar{\Lambda}e^\xi g_{\mu\nu}$, is the potential energy term $V(\xi)$. Moreover, since by construction $\xi(x)$ and $\chi(x)$ are not dynamical fields, variations of the action of the considered theory with respect to $\xi(x)$ and $\chi(x)$ are not required. Therefore, the required action of the theory will finally take the following form:

$$\mathcal{S} = \int d^4x \sqrt{-g} F(\xi) [R - \omega(\xi_{;\mu})^2 - V(\xi) + 16\pi G(x)\mathcal{L}_m]. \quad (13)$$

The variation of this action (13) with respect to $g_{\mu\nu}$ gives

$$\begin{aligned} G_{\mu\nu} &= 8\pi GT_{\mu\nu} - \frac{1}{2}V(\xi)g_{\mu\nu} + \left(\omega + \frac{F''}{F}\right)\xi_{;\mu}\xi_{;\nu} - g_{\mu\nu}\left(\frac{\omega}{2} + \frac{F''}{F}\right)(\xi_{;\mu})^2 \\ &+ \frac{F'}{F}(\xi_{;\mu;\nu} - g_{\mu\nu}\square\xi). \end{aligned} \quad (14)$$

Substituting, $F(\xi) = e^\xi$, $\omega = -3/2$ and $V(x) = 2\bar{\Lambda}e^\xi$ in Eq. (14) and after a few simplifications we will recover the field Eq. (9). Since the field equations follow from a well defined action, the theory admits a consistent EFT interpretation. In the next section, we solve the field equations (9) for a Schwarzschild-(A)dS like BHs within this EFT framework.

III. RENORMALISATION GROUP IMPROVED BLACK HOLE SOLUTION

In this section, we solve the field equations (9) in the vacuum to obtain a BH solution. In Eq. (9), $\xi(x)$ is a predefined spacetime function; therefore, its functional form depends on the underlying spacetime structure. For the Schwarzschild case, the Kretschmann scalar K depends on the RG scale k as follows [78, 79]:

$$K \propto k^4 \quad (15)$$

Again,

$$K = R_{\mu\nu\sigma\rho}R^{\mu\nu\sigma\rho} = \frac{48M^2}{r^6}, \quad (16)$$

where M is the mass parameter and $R_{\mu\nu\sigma\rho}$ is the curvature tensor. Therefore, one can consider

$$k \propto K^{\frac{1}{4}} = \left(\frac{48M^2}{r^6}\right)^{\frac{1}{4}}. \quad (17)$$

This leads to write,

$$k^2 \propto \frac{M}{r^3} = \frac{\zeta M}{r^3}, \quad (18)$$

where ζ is a proportionality constant. The mass parameter M is kept explicit because the curvature of spacetime is produced by the BH mass. Moreover, for the Schwarzschild-(A)dS spacetime, the Kretschmann scalar contains both a mass dependent contribution and a cosmological constant contributions as

$$K = \frac{48M^2}{r^6} + \frac{8}{3}\Lambda^2. \quad (19)$$

Therefore, we decompose the RG scale into a constant asymptotic part, k_0 , accounting for the Λ^2 term [79], and a radial contribution sourced by the BH mass, as given in Eq. (18). Hence, the RG scale for the Schwarzschild-(A)dS spacetime takes form:

$$k^2 = k_0^2 + \frac{\zeta M}{r^3}. \quad (20)$$

It is evident that the cosmological constant $\Lambda(k)$ depends on the RG scale k as $\Lambda(k) \propto k^2$. Comparing this scaling with the parametrization $\Lambda = \bar{\Lambda}e^\xi$ shows that $\xi(x)$ can be identified as

$$\xi = \ln k^2 + \ln(C\bar{\Lambda}^{-1}), \quad (21)$$

where C is a constant and can be absorbed into a redefinition of $\bar{\Lambda}$. Thus, $\xi(x)$ can be define as

$$\xi = \ln k^2. \quad (22)$$

Substituting Eq. (20) in Eq. (22), $\xi(x)$ can be written as

$$\xi = \ln \left(k_0^2 + \frac{\zeta M}{r^3} \right). \quad (23)$$

Expanding Eq. (23) in powers of $1/r$, one can find,

$$\xi = \ln k_0^2 + \frac{\zeta M}{k_0^2 r^3} - \frac{1}{2} \frac{\zeta^2 M^2}{k_0^4 r^6} + O\left(\frac{\zeta^3 M^3}{k_0^6 r^9}\right). \quad (24)$$

Further, Eq. (24) can be rewritten as

$$\xi = \xi_0 + \frac{\epsilon}{r^3} - \frac{1}{2} \frac{\epsilon^2}{r^6} + O\left(\frac{\epsilon^3}{r^9}\right), \quad (25)$$

where $\xi_0 = \ln k_0^2$ and $\epsilon = \zeta M/k_0^2$. The parameter $\epsilon = \zeta M/k_0^2$ controls the strength of the RG induced corrections to the classical geometry. The perturbative solution obtained in this work is valid in the regime $\epsilon \ll 1$, for which the RG corrections represent a small deformation of the Schwarzschild-(A)dS spacetime. In this regime, higher-order terms in the expansion of ξ and the metric functions are parametrically suppressed, ensuring the consistency of the perturbative approach. Consequently, the present analysis does not probe the strong quantum gravity regime near the singularity, but rather captures leading-order RG effects in the semiclassical domain. Since $\bar{\Lambda}$ is taken as a reference value of the cosmological constant in the EFT framework, we treat it as the cosmological constant in the IR limit and consider small values of $\bar{\Lambda}$ of order 10^{-3} in our analysis.

For a spherically symmetric spacetime, we consider the following ansatz:

$$ds^2 = -f(r) dt^2 + \frac{1}{f(r)} dr^2 + r^2 d\Omega, \quad (26)$$

where $d\Omega = d\theta^2 + \sin^2\theta d\phi^2$ and

$$f(r) = f_0(r) + \sum_{i=1}^{\infty} \epsilon^i a_i(r) \quad (27)$$

with

$$f_0(r) = 1 - \frac{2M}{r} - \frac{\bar{\Lambda}}{3} r^2. \quad (28)$$

Here, $f_0(r)$ represents the Schwarzschild-(A)dS solution of GR expressed in terms of the IR cosmological constant $\bar{\Lambda}$, where $\bar{\Lambda} > 0$ corresponds to the SdS case and $\bar{\Lambda} < 0$ to the SAdS case. The second term in $f(r)$ represents perturbative corrections. The function $f(r)$ is expanded as a power series in the parameter ϵ , with the coefficient functions $a_i(r)$ encoding successive higher-order deviations from the GR background. Now, our task is to determine the functions $a_i(r)$ by solving the field equations (9) order by order in the perturbative expansion.

For the first order correction $f(r)$ will have the form:

$$f(r) = f_0(r) + \epsilon a_1(r). \quad (29)$$

For vacuum, i.e., for $T_{\mu\nu} = 0$, Eq. (9) reduces as

$$G_{\mu\nu} = -\bar{\Lambda} e^\xi g_{\mu\nu} - \frac{1}{2} \xi_{;\mu} \xi_{;\nu} - \frac{1}{4} g_{\mu\nu} (\xi_{;\mu})^2 + \xi_{;\mu;\nu} - g_{\mu\nu} \square \xi, \quad (30)$$

where the Einstein tensor on the left-hand side (LHS) has the following forms for the tt , rr and $\theta\theta$ components with the metric (26):

$$G_{tt} = -f \frac{r f' + f - 1}{r^2}, \quad (31)$$

$$G_{rr} = \frac{1}{f} \frac{r f' + f - 1}{r^2}, \quad (32)$$

$$G_{\theta\theta} = \frac{r^2 f''}{2} + r f'. \quad (33)$$

Here, primes denote the differentiation with respect to r . Using the definition of $\xi(x)$ in Eq. (25) upto 1st-order in ϵ , the different terms of the right-hand side (RHS) of Eq. (30) for the $\theta\theta$ component can be written as follows:

$$-\bar{\Lambda}e^\xi g_{\theta\theta} = -\bar{\Lambda}e^{\xi_0}r^2 \left(1 + \frac{\epsilon}{r^3}\right), \quad (34)$$

$$\xi_{;\theta;\theta} = -\frac{3\epsilon f_0}{r^3}, \quad (35)$$

$$-g_{\theta\theta}\square\xi = -\epsilon \left(\frac{6f_0}{r^3} - \frac{3f'_0}{r^2}\right). \quad (36)$$

Further, the second and third terms on the right-hand side of Eq. (30) involve the square of the gradient of ξ . Since the first derivative of ξ is already of first order in the perturbative parameter ϵ , these terms are of the $\mathcal{O}(\epsilon^2)$ and therefore do not contribute at first order in the perturbative expansion. Thus, for $\theta\theta$ component the RHS of Eq. (30) takes the form:

$$\text{RHS}_{\theta\theta} = -\bar{\Lambda}e^{\xi_0}r^2 + \epsilon \left(-\frac{\bar{\Lambda}e^{\xi_0}}{r} - \frac{3f_0}{r^3} + \frac{3f'_0}{r^2}\right). \quad (37)$$

Moreover, as $\bar{\Lambda}$ is an arbitrary reference value, the constant factor e^{ξ_0} can be absorbed into the redefinition of $\bar{\Lambda}$. Hence, Eq. (37) can be written as

$$\text{RHS}_{\theta\theta} = -\bar{\Lambda}r^2 + \epsilon \left(-\frac{\bar{\Lambda}}{r} - \frac{9f_0}{r^3} + \frac{3f'_0}{r^2}\right). \quad (38)$$

Substituting Eq. (29) in Eq. (33), the $G_{\theta\theta}$ component can be expanded upto 1st-order in ϵ as

$$G_{\theta\theta} = \frac{r^2 f''_0}{2} + r f'_0 + \epsilon \left(\frac{r^2}{2} a''_1 + r a'_1\right). \quad (39)$$

Finally, the $\theta\theta$ component of Eq. (30) can be written as

$$\frac{r^2 f''_0}{2} + r f'_0 + \epsilon \left(\frac{r^2}{2} a''_1 + r a'_1\right) = -\bar{\Lambda}r^2 + \epsilon \left(-\frac{\bar{\Lambda}}{r} - \frac{9f_0}{r^3} + \frac{3f'_0}{r^2}\right). \quad (40)$$

Equating the coefficients of ϵ on both sides of Eq. (40) yields the following 1st-order differential equation:

$$\frac{r^2}{2} a''_1 + r a'_1 = -\frac{\bar{\Lambda}}{r} - \frac{9f_0}{r^3} + \frac{3f'_0}{r^2}. \quad (41)$$

Again, substitution of f_0 and f'_0 from Eq. (28), this Eq. (41) reduces as

$$\frac{r^2}{2} a''_1 + r a'_1 = -\frac{9}{r^3} + \frac{24M}{r^4}. \quad (42)$$

Solving this Eq. (42), a_1 can be obtain as

$$a_1(r) = -\frac{3}{r^3} + \frac{4M}{r^4} - \frac{C_1}{r} + C_2, \quad (43)$$

where C_1 and C_2 are constants of integration. In the asymptotic limit $r \rightarrow \infty$, the metric function behaves as

$$f(r) \rightarrow 1 - \frac{\bar{\Lambda}}{3}r^2, \quad (44)$$

which corresponds to the standard asymptotic structure of an (A)dS spacetime. To ensure that the obtained solution preserves this asymptotic behavior, the integration constant C_2 must vanish. Further, the term $\frac{C_1}{r}$ contributes to the coefficient of the $1/r$ term in the metric function, which is directly associated with the ADM mass of the spacetime. Therefore, a non-zero value of C_1 would effectively lead to a redefinition of the mass parameter M . To maintain the physical interpretation of M as the ADM mass of the BH, we impose the regularity condition $C_1 = 0$. Therefore, the RG improved BH solution upto 1st-order in ϵ is as follows:

$$f(r) = 1 - \frac{2M}{r} - \frac{\bar{\Lambda}}{3}r^2 + \epsilon \left(-\frac{3}{r^3} + \frac{4M}{r^4}\right). \quad (45)$$

Following the same process, the BH solution up to 2nd-order in ϵ can be obtained as

$$f(r) = 1 - \frac{2M}{r} - \frac{\bar{\Lambda}}{3} r^2 + \epsilon \left(-\frac{3}{r^3} + \frac{4M}{r^4} \right) + \epsilon^2 \left(\frac{21}{20r^6} - \frac{25M}{14r^7} - \frac{13\bar{\Lambda}}{24r^4} \right). \quad (46)$$

Similarly, higher-order corrections can be systematically obtained by following the same procedure. Since the solution is perturbative, with $\epsilon \ll 1$, contributions from higher-order terms are increasingly suppressed. Hence, we limit our analysis to the second-order solution.

IV. QUASINORMAL MODES OF RENORMALISATION GROUP IMPROVED BLACK HOLES

In this section, we investigate the QNMs of the BH solution presented in Eq. (46) for both SdS and SAdS spacetimes. The analysis is carried out for massless scalar field perturbations propagating in the background of the BH spacetime.

For a massless scalar field Φ the equation of motion is given by [80]

$$\frac{1}{\sqrt{-g}} \partial_\mu (\sqrt{-g} g^{\mu\nu} \partial_\nu \Phi) = 0. \quad (47)$$

Assuming a spherical symmetry, the scalar field Φ can be decomposed into a radial part $R_{\omega,l}(r)$ and an angular part described by the spherical harmonics $Y_l(\theta, \phi)$, and can be expressed as

$$\Phi = e^{\pm i\omega t} \frac{\Psi_{\omega,l}(r)}{r} Y_l(\theta, \phi), \quad (48)$$

where l denotes the multipole number, ω is the frequency of oscillation, and $\Psi_{\omega,l}(r)$ can be defined as

$$\Psi_{\omega,l}(r) = r R_{\omega,l}(r). \quad (49)$$

By substituting Eq. (48) into Eq. (47), we obtain the following Schrödinger-like equation:

$$\frac{d^2 \Psi}{dr_\star^2} + (\omega^2 - V(r)) \Psi = 0, \quad (50)$$

where r_\star denotes the tortoise coordinate, which is defined as

$$r_\star = \int \frac{dr}{f(r)}, \quad (51)$$

and $V(r)$ is the effective potential as given by

$$V(r) = f(r) \left(\frac{f'(r)}{r} + \frac{l(l+1)}{r^2} \right). \quad (52)$$

For an asymptotically flat spacetime, Eq. (50) must satisfy the following boundary conditions:

$$\Psi(r_\star) \rightarrow \begin{cases} A e^{+i\omega r_\star}, & \text{as } r_\star \rightarrow -\infty, \\ B e^{-i\omega r_\star}, & \text{as } r_\star \rightarrow +\infty. \end{cases} \quad (53)$$

Here, A and B represent the amplitudes of the respective wave components. These two conditions respectively correspond to purely ingoing waves at the BH event horizon and purely outgoing waves at spatial infinity, embodying the physical requirement that no information can escape from the horizon and no radiation can originate from infinity. The imposition of these boundary conditions results in an infinite, discrete set of complex frequencies, which are identified as the QNMs of the BH.

A. QNMs in Schwarzschild-de Sitter spacetime

The SdS spacetime describes a Universe with a positive cosmological constant. It features both a BH event horizon and a cosmological horizon [81–83]. In this section, we study the QNMs of the BH described by Eq. (46) for a positive cosmological constant corresponding to the SdS spacetime.

Figure 1 illustrates the behaviour of the effective potential $V(r)$ as a function of the radial coordinate r for different values of the parameter ζ in the SdS case. The left panel shows that positive values of ζ lower the peak of the potential compared to the GR case. This indicates that positive RG corrections lower the effective potential barrier experienced by perturbations. In contrast, the right panel illustrates that for negative values of ζ , the peak of the potential is higher than the GR case, indicating stronger trapping of perturbative modes near the potential maximum. The dependence of $V(r)$ on r for different magnitudes and signs of ζ indicates a clear sensitivity of the QNM spectrum to RG improved corrections. In all the numerical analyses presented in this work, the parameters M , ζ , and k_0 are chosen such that the quantity $\epsilon = \zeta M/k_0^2$ remains $\ll 1$, ensuring the validity of the perturbative approach. Since k_0 represents the asymptotic value of the RG scale $k(r)$ in the limit $r \rightarrow \infty$, i.e. value of $k(r)$ in the IR energy scale and the precise numerical value of it is not fixed by the EFT, we must instead choose its value within a physically reasonable range. In geometrized units, values of $k_0 \sim 1$ – 10 correspond to very low energy scales in conventional units and therefore lie firmly in the IR regime. As the validity of the perturbative analysis requires the parameter $\epsilon \ll 1$, we fix $k_0 = 10$ in our analysis and treat ζ as a free parameter of the theory, choosing its values such that the condition $\epsilon \ll 1$ is satisfied.

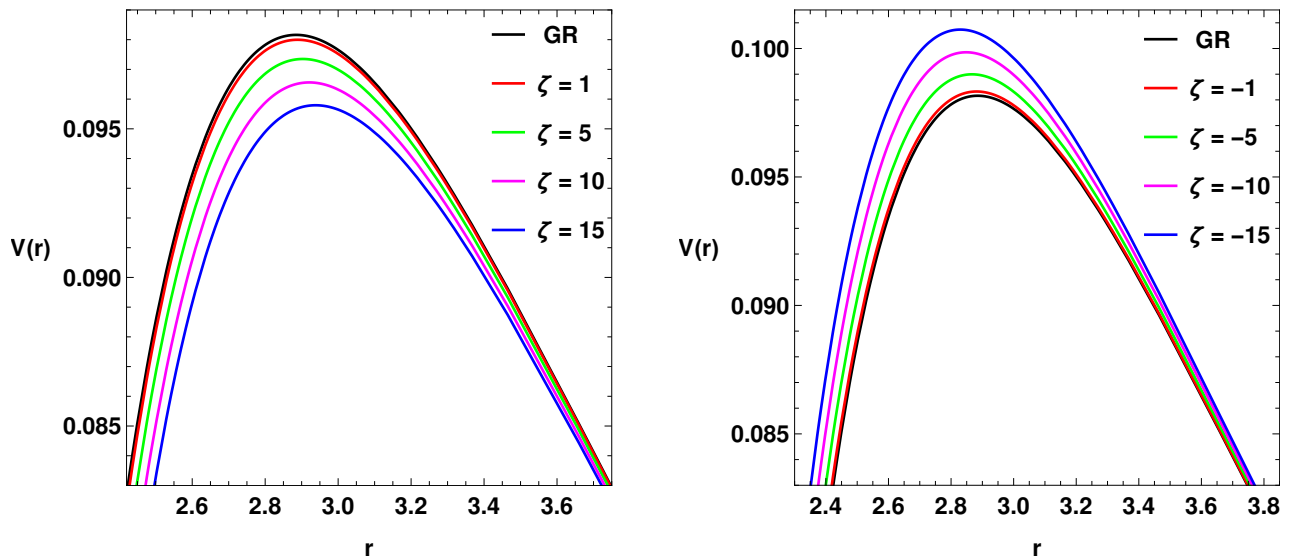


FIG. 1. Behaviour of the effective potential $V(r)$ as a function of the radial coordinate r for both positive and negative values of the parameter ζ , obtained by fixing $M = 1$ and $\bar{\Lambda} = 0.001$.

We compute the QNMs using the 6th-order Padé-averaged WKB approximation method, characterizing them in terms of their oscillation frequency and damping rate, and analyze their dependence on the parameter ζ . Table I presents the QNMs frequencies for different positive values of ζ and for multipole numbers $l = 1, 2, 3$. It can be observed from Table I that both the oscillation frequency and the damping rate decrease as the parameter ζ increases for each value of l . The deviation from the GR case remains small, as expected for small perturbative quantum corrections. Further, for positive values of the parameter ζ , the real part of the QNMs increases with l , while the imaginary part decreases as l increases. Table II displays the QNM frequencies for different negative values of the parameter ζ and for multipole numbers $l = 1, 2, 3$. From Table II, it is evident that both the oscillation frequency and the damping rate increase as ζ is increased within the negative parameter regime for each value of l . Moreover, the dependence of the real and imaginary parts of the QNMs on l for negative values of ζ is the same as that for positive values of ζ . The error associated with the QNMs obtained from the 6th order Padé averaged WKB method is calculated using the formula:

$$\Delta_6 = \frac{|\text{Padé averaged WKB}_7 - \text{Padé averaged WKB}_5|}{2}. \quad (54)$$

Figure 2 illustrates the behaviour of the real and imaginary parts of the QNMs as functions of positive values of the parameter ζ . The left panel shows the variation of the real part of the QNMs, while the right panel displays the variation of the imaginary part of the QNMs with respect to ζ . It can be observed from the figure that both oscillation and damping decrease with the values of ζ . Further, for negative values of the parameter ζ , Fig. 3 shows the variation of the real and imaginary parts of the QNMs with respect to negative values of ζ . In this case, the left panel indicates that the real part of the QNMs increases with increasing negative values of ζ , while the right panel shows a corresponding increase in the imaginary part.

TABLE I. QNMs of BHs described by the solution (46), computed using the 6th-order Padé-averaged WKB approximation method for different positive values of the parameter ζ , with $M = 1$, $n = 0$ and $\bar{\Lambda} = 0.001$.

Multipole	ζ	Padé averaged 6th-order WKB	Δ_6	
GR ($l = 1$)	0	$0.291340 - 0.097472i$	0.3140×10^{-5}	
	1	$0.291058 - 0.097442i$	0.0261×10^{-5}	
	$l = 1$	5	$0.289942 - 0.097328i$	0.0150×10^{-5}
		10	$0.288574 - 0.097194i$	0.0124×10^{-4}
		15	$0.287235 - 0.097067i$	0.3463×10^{-6}
GR ($l = 2$)	0	$0.481284 - 0.0963911i$	0.5298×10^{-4}	
	1	$0.480829 - 0.096352i$	0.0175×10^{-4}	
	$l = 2$	5	$0.479032 - 0.096200i$	0.0256×10^{-5}
		10	$0.476832 - 0.096018i$	0.0128×10^{-6}
		15	$0.474682 - 0.095846i$	0.1524×10^{-6}
GR ($l = 3$)	0	$0.672188 - 0.0960977i$	0.4719×10^{-3}	
	1	$0.671556 - 0.096059i$	0.0152×10^{-5}	
	$l = 3$	5	$0.669059 - 0.095911i$	0.0351×10^{-5}
		10	$0.666003 - 0.095734i$	0.5420×10^{-5}
		15	$0.663016 - 0.095565i$	0.01269×10^{-4}

TABLE II. QNMs of BHs described by the solution (46), computed using the 6th-order Padé-averaged WKB approximation method for different negative values of the parameter ζ , with $M = 1$, $n = 0$ and $\bar{\Lambda} = 0.001$.

Multipole	ζ	Padé averaged 6th-order WKB	Δ_6
$l = 1$	-1	$0.291624 - 0.097502i$	0.1430×10^{-5}
	-5	$0.292770 - 0.097625i$	0.0325×10^{-5}
	-10	$0.294231 - 0.097789i$	0.0325×10^{-5}
	-15	$0.295727 - 0.097963i$	0.1035×10^{-4}
$l = 2$	-1	$0.481740 - 0.096430i$	0.0238×10^{-4}
	-5	$0.483589 - 0.096592i$	0.5416×10^{-5}
	-10	$0.485951 - 0.096806i$	0.0023×10^{-5}
	-15	$0.488371 - 0.097034i$	0.0362×10^{-5}
$l = 3$	-1	$0.672822 - 0.096136i$	0.0023×10^{-5}
	-5	$0.675391 - 0.096293i$	0.4521×10^{-5}
	-10	$0.678673 - 0.096501i$	0.0105×10^{-5}
	-15	$0.682036 - 0.096721i$	0.3015×10^{-4}

B. QNMs in Schwarzschild-Anti-de Sitter spacetime

The SAdS spacetime describes a BH embedded in a background with a negative cosmological constant. In contrast to the SdS case, spacetime possesses only a BH event horizon, while the SAdS boundary at spatial infinity plays an important role in determining the global structure and dynamical properties of spacetime. In this section, we study the QNMs of BHs described by solution (46) for a negative cosmological constant corresponding to the SAdS spacetime. In SAdS geometries, the perturbation equations possess regular singular points at both the event horizon and at spatial infinity. The tortoise coordinate r_* diverges to $-\infty$ as $r \rightarrow r_h$, where r_h denotes the event horizon radius, while r_* approaches a finite constant as $r \rightarrow \infty$ [84]. Moreover, since in the SAdS spacetime the tortoise coordinate r_* approaches a finite constant as $r \rightarrow \infty$ [84], consequently, the boundary conditions required for QNMs differ from the asymptotically flat or SdS spacetime. However, the condition at the event horizon remains the same: only purely ingoing modes are allowed, so that

$$\Psi(r_*) \rightarrow A e^{i\omega r_*}, \quad r_* \rightarrow -\infty. \quad (55)$$

At spatial infinity, the scalar field perturbation Eq. (50) yields the asymptotic behaviour as

$$\Psi \sim C r^{-2} + D r, \quad r \rightarrow \infty. \quad (56)$$

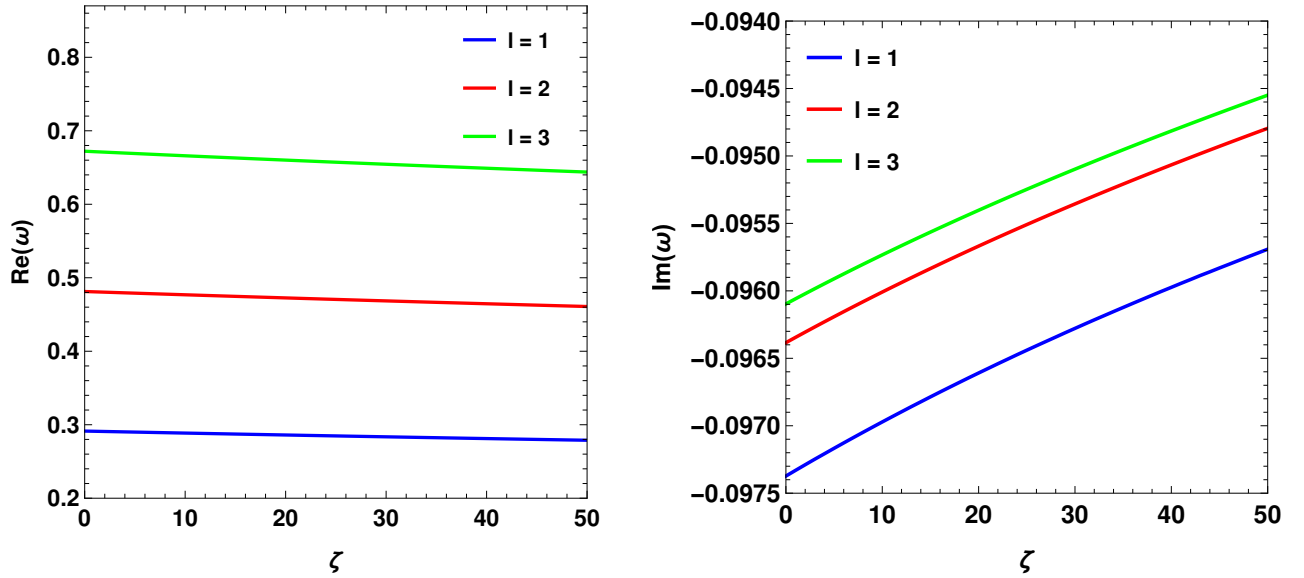


FIG. 2. Variation of real and imaginary parts of QNMs with respect to positive values of ζ for different values of l along with $M = 1$, $n = 0$ and $\bar{\Lambda} = 0.001$.

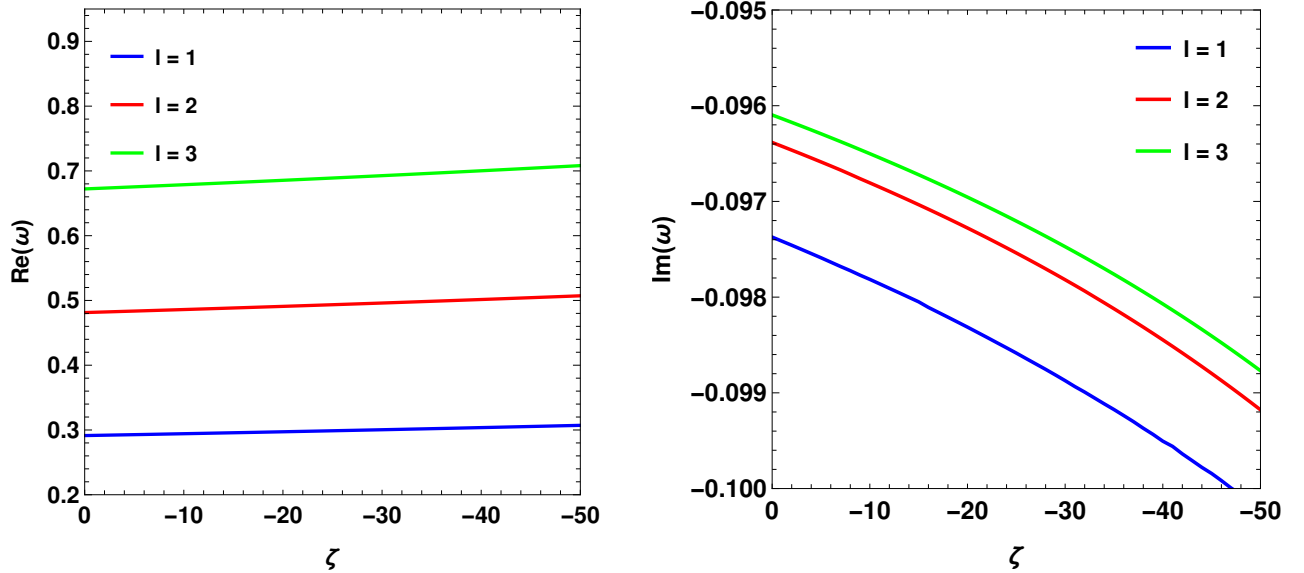


FIG. 3. Variation of real and imaginary parts of QNMs with respect to negative values of ζ for different values of l along with $M = 1$, $n = 0$ and $\bar{\Lambda} = 0.001$.

Here, C and D are two constant coefficients. Regularity of the scalar field at the SAdS boundary requires the absence of the divergent term, implying $D = 0$. This corresponds to imposing a Dirichlet boundary condition at infinity for determining the QNMs.

Fig. 4 shows the variation of $V(r)$ with respect to r for different values of ζ in SAdS BH spacetime. The left panel corresponds to positive values of ζ . It is clear from the left panel that, for positive values of ζ , the peak of the effective potential decreases as ζ increases. The right panel shows that, for negative values of ζ , the height of the potential increases as negative values of ζ increase.

The WKB approximation cannot be reliably applied to SAdS spacetimes because the SAdS boundary at spatial infinity is reflective rather than purely outgoing. Therefore, in this section, we compute the QNMs using the direct shooting method described in Refs. [85–88]. The radial equation is integrated outward from the horizon with the ingoing boundary condition. At large radius, the solution behaves as $\Psi(r) = Ar + B/r^{l+1}$, and the QNMs are obtained by imposing the Dirichlet boundary condition $A = 0$. The uncertainty of the QNM frequencies is estimated from the numerical stability of the shooting procedure. For a fixed value of the parameter ζ , the computation is repeated by varying the asymptotic radius, the integration domain, and

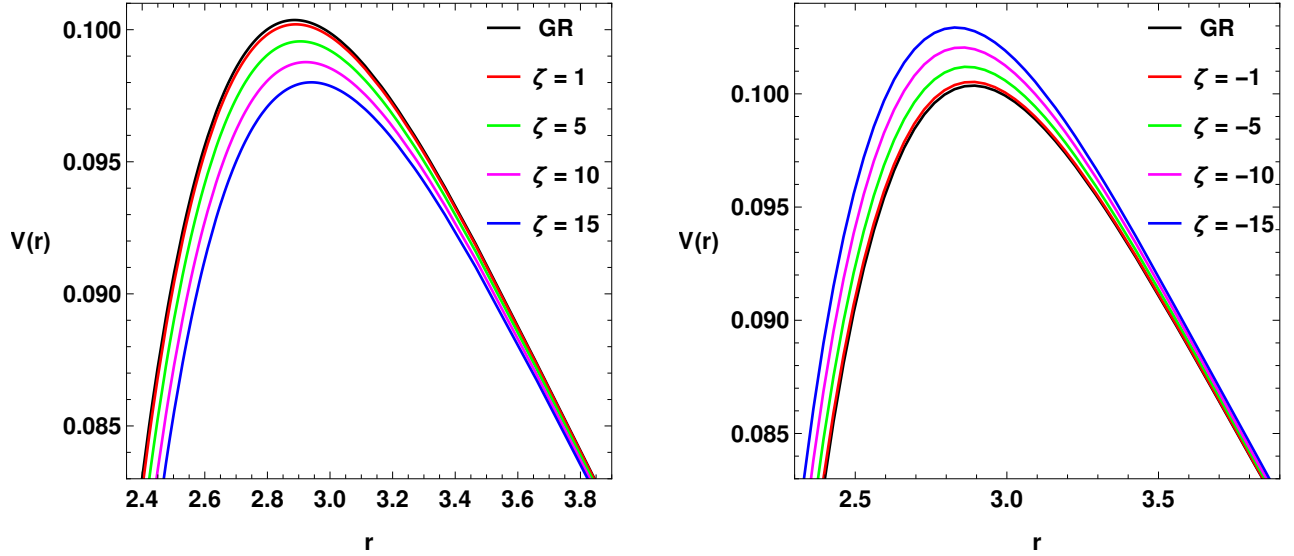


FIG. 4. Behaviour of the effective potential $V(r)$ as a function of the radial coordinate r for both positive and negative values of ζ , fixing $M = 1$, and $\bar{\Lambda} = -0.001$.

the solver accuracy. The frequency is found to be stable up to six decimal places under these variations. Therefore, the results are used up to six decimal places.

Table III shows the variation of the QNMs with respect to both positive and negative values of ζ for different values of l . It can be observed from the table that for each l , both real and imaginary part of the QNMs increases for positive values of ζ . On the other hand, for negative values of ζ , both real and imaginary part of QNMs decreases with the increasing negative values of ζ . Further, as l increases, both real and imaginary parts increase monotonically. Moreover, similar to the SdS case, the variation of the QNMs with respect to ζ is small for low values of ζ , and becomes more prominent for larger ζ .

TABLE III. QNMs of BHs described by the solution (46), computed using the Direct Shooting Method for both positive and negative values of the parameter ζ , with $n = 0$, $M = 1$ and $\bar{\Lambda} = -0.001$.

Multipole	ζ	Direct Shooting Method	ζ	Direct Shooting Method
GR ($l = 1$)	0	$0.381323 - 0.034391i$	0	$0.381323 - 0.034391i$
$l = 1$	1	$0.381359 - 0.034444i$	-1	$0.381287 - 0.034338i$
	7	$0.381572 - 0.034757i$	-7	$0.381067 - 0.034014i$
	14	$0.381814 - 0.035112i$	-14	$0.380805 - 0.033626i$
	21	$0.382051 - 0.035458i$	-21	$0.380536 - 0.033224i$
GR ($l = 2$)	0	$0.489696 - 0.038371i$	0	$0.489696 - 0.038371i$
$l = 2$	1	$0.489727 - 0.038411i$	-1	$0.489666 - 0.038332i$
	7	$0.489908 - 0.038645i$	-7	$0.489480 - 0.038089i$
	14	$0.490115 - 0.038909i$	-14	$0.489258 - 0.037796i$
	21	$0.490318 - 0.039166i$	-21	$0.489032 - 0.037492i$
GR ($l = 3$)	0	$0.673089 - 0.045701i$	0	$0.673089 - 0.045701i$
$l = 3$	1	$0.673131 - 0.045771i$	-1	$0.673046 - 0.045629i$
	7	$0.673381 - 0.046190i$	-7	$0.672790 - 0.045194i$
	14	$0.673666 - 0.046665i$	-14	$0.672484 - 0.044671i$
	21	$0.673943 - 0.047126i$	-21	$0.672174 - 0.044129i$

For visual realization, Fig. 5 shows the variation of the real and imaginary parts of the QNMs with respect to positive values of ζ . It is clear from the figure that both real and the imaginary part increases as ζ increases. Similarly, Fig. 6 shows the variation of the QNMs for negative values of ζ . As seen in Fig. 6, the both real and the imaginary part decreases with the values of ζ , for each l .

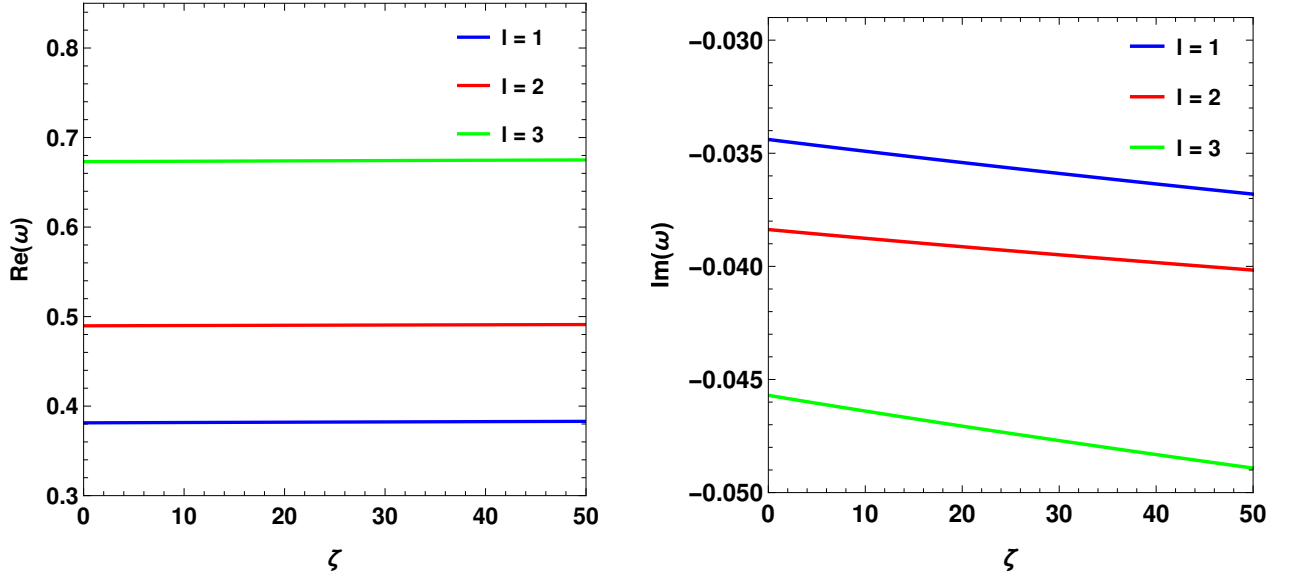


FIG. 5. Variation of real and imaginary parts of QNMs with respect to positive values of ζ for different values of l along with $M = 1$, $n = 0$, and $\bar{\Lambda} = -0.001$.

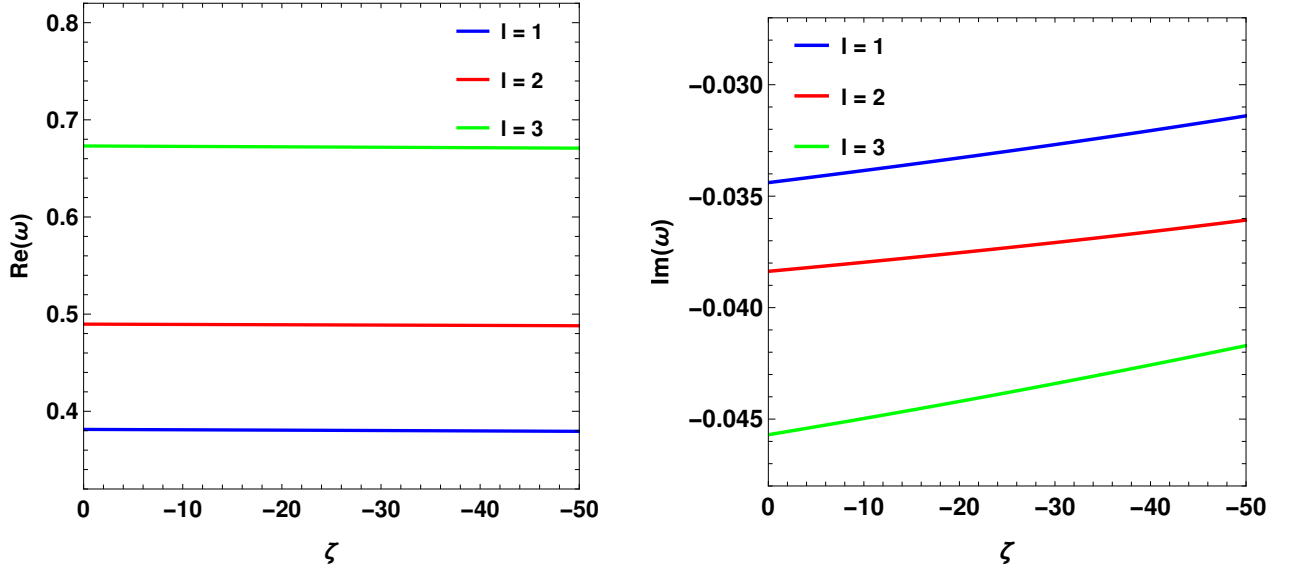


FIG. 6. Variation of real and imaginary parts of QNMs with respect to negative values of ζ for different values of l along with $M = 1$, $n = 0$, and $\bar{\Lambda} = -0.001$.

V. EVOLUTION OF SCALAR PERTURBATIONS AROUND THE BLACK HOLES

In this section, we investigate the time evolution of scalar field perturbations in the BH spacetimes described by the solution (46), for both SdS and SAdS spacetimes. For this purpose, we employ the time-domain integration method described in Refs. [89, 90]. Accordingly, defining $\Psi(r_*, t) = \Psi(i \Delta r_*, j \Delta t) = \Psi_{i,j}$ and $V(r(r_*)) = V(r_*, t) = V_{i,j}$, Eq. (50) can be written in the following form:

$$\frac{\Psi_{i+1,j} - 2\Psi_{i,j} + \Psi_{i-1,j}}{\Delta r_*^2} - \frac{\Psi_{i,j+1} - 2\Psi_{i,j} + \Psi_{i,j-1}}{\Delta t^2} - V_i \Psi_{i,j} = 0. \quad (57)$$

Now, using the initial conditions: $\Psi(r_*, t) = \exp[-(r_* - q)^2/2\sigma^2]$ and $|\Psi(r_*, t)|_{t<0} = 0$, where q is the median and σ is the width of the initial wave packet, the time evolution of the scalar field can finally be written as

$$\Psi_{i,j+1} = -\Psi_{i,j-1} + \left(\frac{\Delta t}{\Delta r_*}\right)^2 (\Psi_{i+1,j} + \Psi_{i-1,j}) + \left(2 - 2\left(\frac{\Delta t}{\Delta r_*}\right)^2 - V_i \Delta t^2\right) \Psi_{i,j}. \quad (58)$$

Moreover, during the numerical procedure, we impose the Von Neumann stability condition $\frac{\Delta t}{\Delta r_*} < 1$ to ensure stable results and compute the time profiles. Fig. 7 illustrates the time-domain profiles of scalar field perturbations in the BH spacetime for

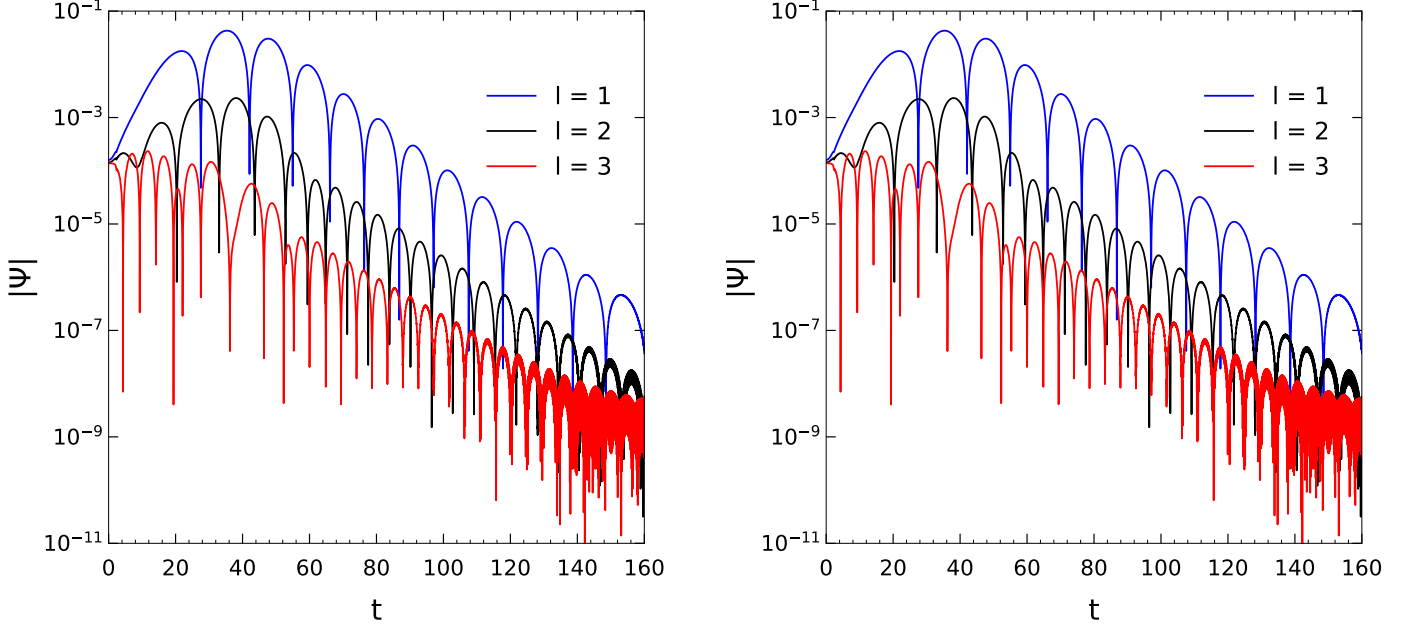


FIG. 7. Time-domain profiles of scalar field perturbations in the BH spacetime described by the metric (46) for the SdS case with $\zeta = 10$ (left plot) and $\zeta = -10$ (right plot). For both plots $\bar{\Lambda} = 0.001$ and $n = 0$ are used.

the SdS case, where the left panel corresponds to $\zeta = 10$, while the right panel corresponds to $\zeta = -10$. The dependence of the oscillation frequency and damping rate of the QNMs on l , discussed in Table I and Table II, is also reflected in Fig. 7. Fig. 8 shows the time-domain profiles of the scalar field perturbations in the SAdS spacetime, where the left panel corresponds to $\zeta = 10$, while the right panel corresponds to $\zeta = -10$. Similar to the SdS case, the dependence of the oscillation and damping behaviour on l is also reflected in the time-domain profile.

Furthermore, we employed the Matrix Pencil (MP) method, as described in Refs. [91–93], to extract the QNMs from the time-domain profiles. For this, from the time profile waveform, first we constructed two time shifted Hankel matrices Y_0 and Y_1 . Then a singular value decomposition (SVD) was performed on Y_1 as $Y_1 = USV^\dagger$, where U and V are unitary matrices containing the left and right singular vectors, respectively, and S is a diagonal matrix whose diagonal entries are the singular values. We kept the largest singular values (say p) corresponding to the physical QNMs and discarded the remaining noise dominated components. The reduced matrices were then used to form the matrix $Z_p = S_p^{-1}U_p^\dagger Y_0 V_p$, here U_p and V_p denote the matrices formed by the first p columns of the left and right singular vector matrices U and V , respectively, while S_p^{-1} is the inverse of the diagonal matrix S_p containing the p largest singular values. The eigenvalues of Z_p provide estimates of the inverse poles of the waveform. From these poles, we obtained the complex frequencies as described in [93], where the real part corresponds to the oscillation frequency and the imaginary part determines the damping rate. Finally, the extracted QNMs were used to reconstruct the time-domain waveform and matched against the original time-domain profile. The coefficient of determination R^2 is computed as

$$R^2 = 1 - \frac{\sum (\psi_{\text{Time-Profile}} - \psi_{\text{MP}})^2}{\sum (\psi_{\text{Time-Profile}} - \bar{\psi}_{\text{Time-Profile}})^2}, \quad (59)$$

where $\psi_{\text{Time-Profile}}$ denotes the amplitude of the original time-domain waveform, ψ_{MP} is the amplitude of the waveform reconstructed using the MP method, and $\bar{\psi}_{\text{Time-Profile}}$ is the mean value of the original time-domain waveform.

Fig. 9 shows a comparison between the waveforms reconstructed using the MP method and the original time-domain profiles for the SdS case. The left panel corresponds to $l = 2$ with $\zeta = 10$, while the right panel corresponds to $l = 3$ with $\zeta = -10$.

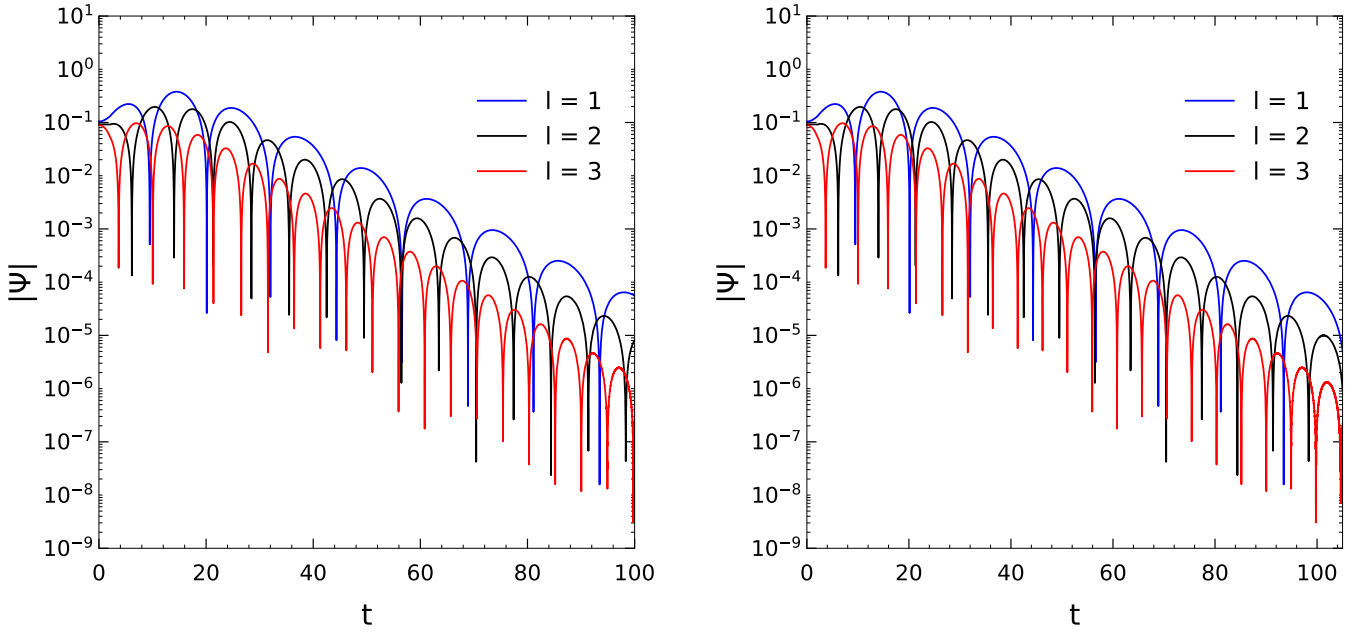


FIG. 8. Time-domain profiles of scalar field perturbations in the BH spacetime described by the metric (46) for the SAdS case with $\zeta = 10$ (left plot) and $\zeta = -10$ (right plot). For both plots $\bar{\Lambda} = -0.001$, and $n = 0$ are used.

It can be seen that the waveform reconstructed from the QNMs extracted via the MP method is in good agreement with the original time-domain waveforms. Table IV presents a comparison between the QNMs extracted from the time-domain profile

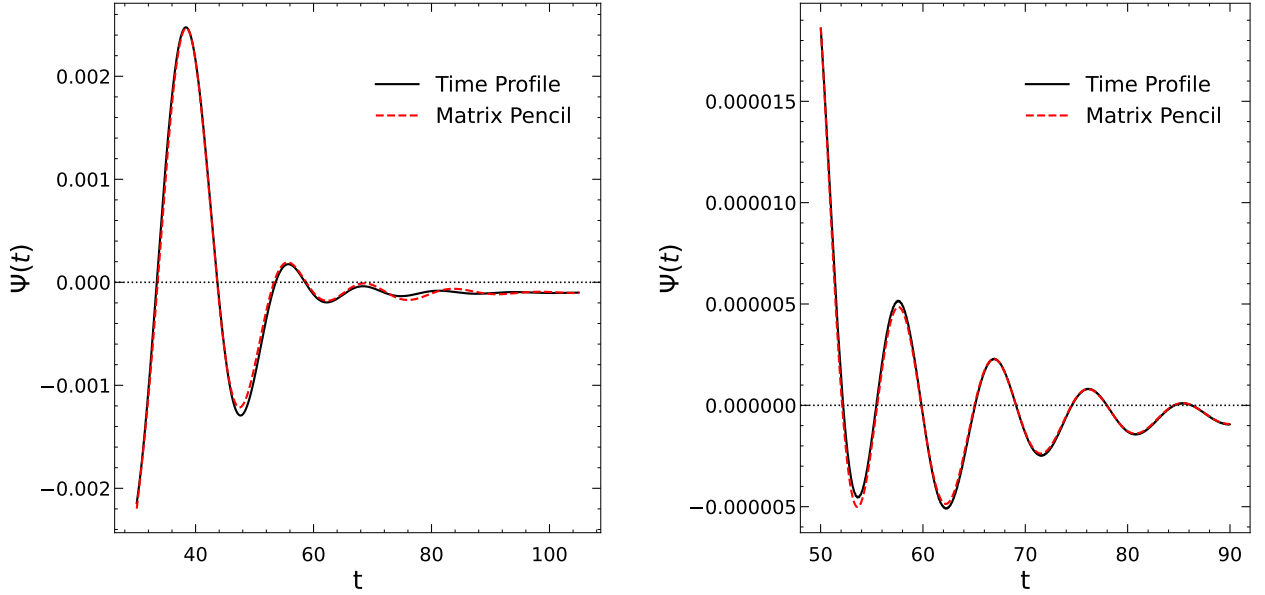


FIG. 9. Comparison between the scalar field QNM time-domain profiles and the waveforms reconstructed using the Matrix Pencil method for the SdS case with $\bar{\Lambda} = 0.001$, and $n = 0$. The left plot is for $l = 2$ with $\zeta = 10$, while the right plot is for $l = 3$ with $\zeta = -10$.

using the MP method and those obtained using the Padé-averaged WKB method for the SdS case. It is evident that the QNMs derived from the time profile are in good agreement with the results from the Padé-averaged WKB approach. We calculate the difference in the magnitudes of the QNMs obtained from the 6th-order Padé averaged WKB approximation method and those obtained from the time domain profile using the MP method as follows:

$$\Delta_{\text{QNM}} = \frac{|\text{QNM}_{\text{WKB}} - \text{QNM}_{\text{Time-Profile}}|}{2}. \quad (60)$$

Moreover, Fig. 10 illustrates a comparison between the waveforms of time-domain profiles and those obtained from the MP

TABLE IV. Comparison of QNMs extracted from the time-domain profiles using the Matrix Pencil method and that obtained from the Padé averaged WKB method.

l	ζ	Time-domain	R^2	Padé averaged WKB	Δ_{QNM}
$l = 1$	3	$0.291762 - 0.097415i$	0.995360	$0.290497 - 0.097385i$	0.000633
$l = 2$	10	$0.472973 - 0.096106i$	0.997538	$0.476832 - 0.096018i$	0.001930
$l = 3$	16	$0.669175 - 0.095286i$	0.998405	$0.662426 - 0.095532i$	0.003377
$l = 1$	-3	$0.294631 - 0.097917i$	0.987225	$0.292194 - 0.097563i$	0.001231
$l = 2$	-10	$0.481760 - 0.096781i$	0.9955785	$0.485951 - 0.096806i$	0.002096
$l = 3$	-16	$0.685193 - 0.096542i$	0.999740	$0.682719 - 0.096767i$	0.001242

method for the SAdS case. The left panel corresponds to $l = 3$ with $\zeta = 10$ and right panel corresponds to $l = 1$ with $\zeta = -10$. The figure clearly shows that, for the SAdS case also the two waveforms are in good agreement. Table V presents

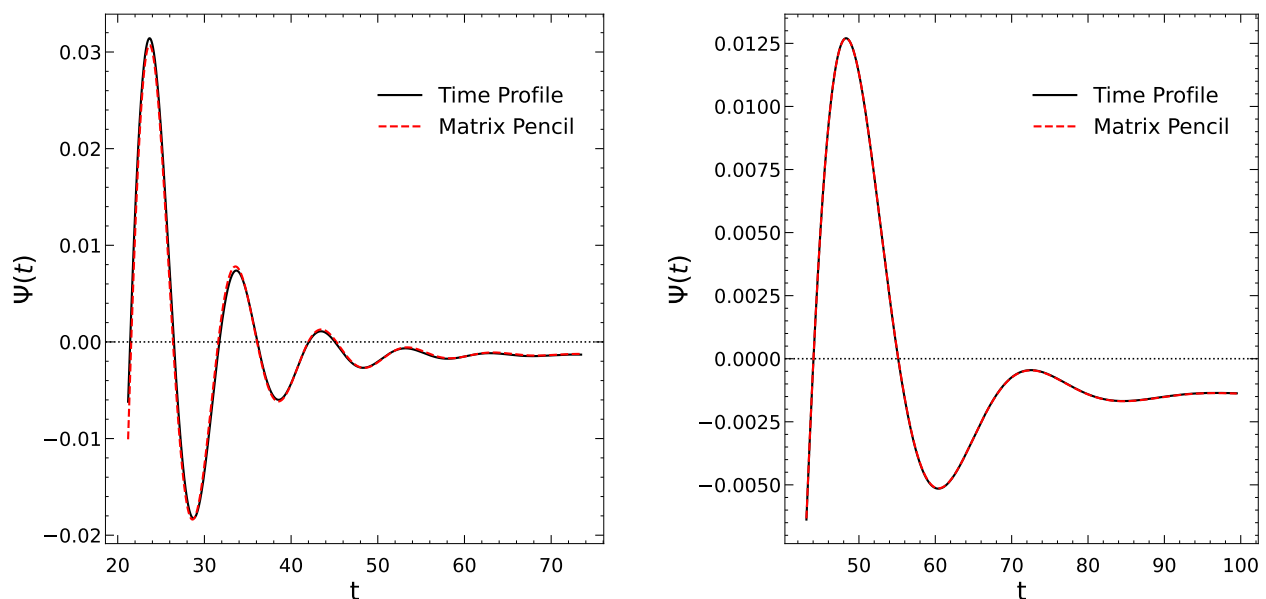


FIG. 10. Comparison between the QNM time-domain profile and the waveform reconstructed using the Matrix Pencil method for the SAdS case with $\bar{\Lambda} = -0.001$, $n = 0$. The left plot is for $l = 3$ with $\zeta = 10$ and the right plot is for $l = 1$ with $\zeta = -10$.

the QNMs obtained from the direct shooting method and those extracted from the time-domain profile for the SAdS case. The close agreement between the two sets of results demonstrates the reliability of our analysis. The difference between the QNMs obtained from the time-domain method and those obtained from the direct shooting method is calculated using

$$\Delta_{\text{QNM}} = \frac{|\text{QNM}_{\text{Direct Shooting}} - \text{QNM}_{\text{Time-Profile}}|}{2}. \quad (61)$$

VI. SUMMERY AND CONCLUSION

The goal of this work is to construct an RG improved perturbative BH solution, and to study the QNMs of the corresponding BHs in both SdS and SAdS spacetimes. The BH solution constructed in this work is an EFT solution, in which low-energy corrections are incorporated into the GR sector. These corrections can encode low-energy QG effects. Studying the QNMs provides insight into the impact of such tiny corrections and possible QG effects.

In Section II, we briefly discuss the RG improved action and the corresponding field equations derived from it, following Refs. [57, 58]. The BH solution is constructed in Section III up to 2nd-order corrections. Since the correction parameter $\epsilon \ll 1$, we truncate the solution at second order as higher-order terms involve higher powers of ϵ and are therefore suppressed.

TABLE V. Comparison of QNMs extracted from the time-domain profiles using the Matrix Pencil method and that obtained from the Direct Shooting method, for the SAdS case.

l	ζ	Time domain	R^2	Direct Shooting method	Δ_{QNM}
$l = 1$	3	$0.388571 - 0.034287i$	0.999360	$0.381430 - 0.034549i$	0.003573
$l = 2$	10	$0.481796 - 0.038596i$	0.991538	$0.489997 - 0.038759i$	0.004101
$l = 3$	16	$0.673482 - 0.046128i$	0.999230	$0.673746 - 0.046798i$	0.000360
$l = 1$	-3	$0.383782 - 0.034487i$	0.998722	$0.381214 - 0.034231i$	0.001290
$l = 2$	-10	$0.489247 - 0.037982i$	0.999982	$0.489385 - 0.037965i$	0.002571
$l = 3$	-16	$0.675792 - 0.044612i$	0.997250	$0.672396 - 0.044518i$	0.001699

The QNMs of the BHs are investigated in Section IV. In this work, we consider a scalar field perturbation and analyze the QNMs for both SdS and SAdS spacetimes. In Subsection IV A, we focus on the SdS spacetime. The behaviour of the reduced potential is examined for different values of ζ with $k_0 = 10$, $M = 1$, and $\bar{\Lambda} = 0.001$. It is found that, for positive values of ζ , the peak of the potential decreases relative to the GR case, whereas for negative values of ζ the peak increases compared to the GR case. The behaviour of the reduced potential with respect to r for different values of ζ is shown in Figure 1. The QNMs are computed using the 6th-order Padé-averaged WKB approximation for different values of ζ . For positive values of ζ , both the real and imaginary parts of the QNMs decrease, whereas for negative values of ζ they increase. Moreover, for both positive and negative ζ , the real parts increases and imaginary parts decreases with the multipole number l . The behaviour of real and imaginary parts of QNMs with respect to ζ and l is shown in Figures 2 and 3 and tabulated in Tables I and II. In subsection IV B, we study the QNMs in the SAdS spacetime using the direct shooting method. The behaviour of the effective potential $V(r)$ in this case as a function of r for different values of ζ is shown in Figure 4. The corresponding QNMs are listed in Table III for both positive and negative values of ζ and for different multipole numbers l . Figure 5 illustrates the variation of real and imaginary parts of QNMs with respect to positive values of ζ , and Figure 6 shows the variation of real and imaginary parts of QNMs with respect to negative values of ζ in SAdS spacetime.

Further, the time evolution of a scalar perturbations is studied in Section 5 for both SdS and SAdS spacetimes. The time-domain profile for the scalar field perturbations is studied using Eq. (58). Figure 7 displays the time-domain profiles of the scalar field perturbations for the SdS case, and Figure 8 shows the time-domain profiles for the SAdS case. The behaviour of oscillation and damping of QNMs with respect to l reflected in the time-domain profile is in good agreement with the Padé-averaged WKB approximation method for the SdS case and direct shooting method for SAdS case. To extract the QNMs from the time profile, we employed the MP method. The extracted QNMs are used to reconstruct the waveforms. In Figure 9 we show the comparison between the original time profile waveforms and the reconstructed waveforms using the QNMs obtained from the MP method, for the SdS case considering $l = 2$ and $l = 3$. Moreover, Table IV illustrates the QNMs obtained from time-domain analysis and Padé-averaged WKB approximation. It can be observed from the table that the QNMs obtained from both methods are in good agreement. Next, we extend this analysis to the SAdS case. Using the same MP method, the QNMs are extracted. The comparison between the extracted waveforms and the original time-domain waveforms is shown in Figure 10 for $l = 3$ and $l = 1$. Table V presents the QNMs obtained from the time-domain analysis and the direct shooting method for different values of l and ζ . For the SAdS case also the QNMs obtained from both methods are in good agreement.

Our study primarily focuses on the effects on QNMs arising from small higher-order corrections to GR due to RG improvement. Such corrections, obtained through RG improvement, can encode tiny QG effects. Studying BH observables such as QNMs can provide a probe to test these QG effects. This work can be extended to other observables, such as the BH shadow and Quasi-Periodic Oscillations (QPO). Overall, this study contributes to the understanding of low-energy QG effects and offers valuable insights for future research.

ACKNOWLEDGEMENTS

UDG is thankful to the Inter-University Centre for Astronomy and Astrophysics (IUCAA), Pune, India for the Visiting Associateship of the institute.

-
- [1] B. P. Abbott et al., *Observation of Gravitational Waves from a Binary Black Hole Merger*, *Phys. Rev. Lett.* **116**, 061102 (2016).
[2] B. P. Abbott et al., *GW151226: Observation of Gravitational Waves from a 22-Solar-Mass Binary Black Hole Coalescence*, *Phys. Rev. Lett.* **116**, 241103 (2016).

- [3] B. P. Abbott et al., *GW170817: Observation of Gravitational Waves from a Binary Neutron Star Inspiral*, *Phys. Rev. Lett.* **119**, 161101 (2017).
- [4] R. Abbott et al., *GW190412: Observation of a Binary-Black-Hole Coalescence with Asymmetric Masses*, *Phys. Rev. D* **102**, 043015 (2020).
- [5] R. Abbott et al., *Observation of Gravitational Waves from Two Neutron Star–Black Hole Coalescences*, *Astrophys. J. Lett.* **915**, L5 (2021).
- [6] The Event Horizon Telescope Collaboration, *First M87 Event Horizon Telescope Results. IV. Imaging the Central Supermassive Black Hole*, *Astrophys. J. Lett.* **875**, L4 (2019).
- [7] The Event Horizon Telescope Collaboration, *First M87 Event Horizon Telescope Results. II. Array and Instrumentation*, *Astrophys. J. Lett.* **875**, L2 (2019).
- [8] The Event Horizon Telescope Collaboration, *First M87 Event Horizon Telescope Results. III. Data Processing and Calibration*, *Astrophys. J. Lett.* **875**, L3 (2019).
- [9] The Event Horizon Telescope Collaboration, *First M87 Event Horizon Telescope Results and the Role of ALMA*, *The Messenger* **177**, 25 (2019).
- [10] The Event Horizon Telescope Collaboration, *First M87 Event Horizon Telescope Results. V. Physical Origin of the Asymmetric Ring*, *Astrophys. J. Lett.* **875**, L5 (2019).
- [11] The Event Horizon Telescope Collaboration, *First M87 Event Horizon Telescope Results. VI. The Shadow and Mass of the Central Black Hole*, *Astrophys. J. Lett.* **875**, L6 (2019).
- [12] A. G. Riess et al., *Observational evidence from supernovae for an accelerating universe and a cosmological constant*, *Astron. J.* **116**, 1009 (1998).
- [13] S. Perlmutter et al., *Measurements of Ω and Λ from 42 High Redshift Supernovae*, *Astrophys. J.* **517**, 565 (1999).
- [14] C. Pérez de los Heros, *Status, Challenges and Directions in Indirect Dark Matter Searches*, *Symmetry* **12**, 1648 (2020).
- [15] N. A. Bahcall et al., *The Cosmic Triangle: Assessing the State of the Universe*, *Science* **284**, 1481 (1999).
- [16] G. Amelino-Camelia, *Are we at the dawn of quantum gravity phenomenology?*, *Lect. Notes Phys.* **541**, 1 (2000).
- [17] R. Gambini et al., *Fundamental decoherence from quantum gravity: A Pedagogical review*, *Gen. Rel. Grav.* **39**, 1143 (2007).
- [18] S. De et al., *Quantum gravity as an emergent phenomenon*, *Int. J. Mod. Phys. D* **28**, 1944003 (2019).
- [19] M. Van Raamsdonk, *Lectures on gravity and entanglement*, *Theor. Adv. Study Inst. Elem. Part. Phys.* **5**, 297 (2017).
- [20] R. Loll, *Quantum Gravity from Causal Dynamical Triangulations: A Review*, *Class. Quant. Grav.* **37**, 013002 (2020).
- [21] J. Oppenheim, *A postquantum theory of classical gravity?*, *Phys. Rev. X* **13**, 041040 (2023).
- [22] A. Ashtekar and E. Bianchi, *A short review of loop quantum gravity*, *Rept. Prog. Phys.* **84**, 042001 (2021).
- [23] C. Rovelli, *Loop quantum gravity*, *Living Rev. Rel.* **1**, 1 (1998).
- [24] H. Sahlmann, *Loop Quantum Gravity - A Short Review*, [arXiv:1001.4188 \[gr-qc\]](https://arxiv.org/abs/1001.4188).
- [25] F. Girelli, F. Hinterleitner, and S. Major, *Loop Quantum Gravity Phenomenology: Linking Loops to Observational Physics*, *SIGMA* **8**, 098 (2012).
- [26] J. L. F. Barbon, *String theory*, *Eur. Phys. J. C* **33**, S67 (2004).
- [27] E. T. Akhmedov, *Review of modern string theory*, *Phys. Atom. Nucl.* **72**, 1574 (2009).
- [28] S. B. Giddings, *Is string theory a theory of quantum gravity?*, *Found. Phys.* **43**, 115 (2013).
- [29] J. Maharana, *Quantum gravity and string theory*, *18th Conference of the Indian Association for General Relativity and Gravitation*, 155 (1996).
- [30] J. Bedford, *An Introduction to String Theory*, [arXiv:1107.3967 \[hep-th\]](https://arxiv.org/abs/1107.3967).
- [31] J. F. Donoghue, *General relativity as an effective field theory: The leading quantum corrections*, *Phys. Rev. D* **50**, 3874 (1994).
- [32] J. F. Donoghue, *Introduction to the effective field theory description of gravity*, [arXiv:gr-qc/9512024](https://arxiv.org/abs/gr-qc/9512024).
- [33] S. Faller, *Effective field theory of gravity: Leading quantum gravitational corrections to Newton's and Coulomb's law*, *Phys. Rev. D* **77**, 124039 (2008).
- [34] L. I. Bevilaqua, A. C. Lehum, and A. J. da Silva, *Effective field theory of quantum gravity coupled to scalar electrodynamics*, *Class. Quant. Grav.* **33**, 095008 (2016).
- [35] D. Wallace, *Quantum Gravity at Low Energies*, [arXiv:2112.12235 \[gr-qc\]](https://arxiv.org/abs/2112.12235).
- [36] J. F. Donoghue and B. R. Holstein, *Low Energy Theorems of Quantum Gravity from Effective Field Theory*, *J. Phys. G* **42**, 103102 (2015).
- [37] V. Cardoso et al., *Black holes in an effective field theory extension of general relativity*, *Phys. Rev. Lett.* **131**, 109903 (2018).
- [38] S. Hollands, A. Ishibashi, and H. S. Reall, *A stationary black hole must be axisymmetric in effective field theory*, *Commun. Math. Phys.* **401**, 2757 (2023).
- [39] S. Bhattacharyya, P. Biswas, A. Dinda, and N. Kundu, *The zeroth law of black hole thermodynamics in arbitrary higher derivative theories of gravity*, *JHEP* **2022**, 13 (2022).
- [40] S. Bhattacharyya et al., *An entropy current and the second law in higher derivative theories of gravity*, *JHEP* **2021**, 169 (2021).
- [41] I. Davies and H. S. Reall, *Dynamical black hole entropy in effective field theory*, *JHEP* **2023**, 006 (2023).
- [42] S. Bhattacharjee, S. Sarkar, and A. C. Wall, *Holographic entropy increases in quadratic curvature gravity*, *Phys. Rev. D* **92**, 064006 (2015).
- [43] F. Serra, *Black Holes through the Lenses of Effective Field Theory*, PhD thesis, Scuola Normale Superiore, Pisa, Italy (2023).
- [44] D. Wu, W. Liu, and J. Wang, *Light rings and shadows of static black holes in effective quantum gravity*, *Phys. Lett. B* **858**, 139052 (2024).
- [45] I. Davies and H. S. Reall, *Nonperturbative second law of black hole mechanics in effective field theory*, *Phys. Rev. Lett.* **132**, 171402 (2024).
- [46] A. Eichhorn, *Asymptotically safe gravity*, in *Proc. 57th International School of Subnuclear Physics: In Search for the Unexpected* (2020).
- [47] G. Lambiase and F. Scardigli, *Generalized uncertainty principle and asymptotically safe gravity*, *Phys. Rev. D* **105**, 124054 (2022).
- [48] J. Daas et al., *Asymptotically safe gravity with fermions*, *Phys. Lett. B* **809**, 135775 (2020).

- [49] M. Niedermaier and M. Reuter, *The asymptotic safety scenario in quantum gravity*, *Living Rev. Relativ.* **9**, 5 (2006).
- [50] A. Eichhorn and A. Held, *Towards implications of asymptotically safe gravity for particle physics*, *PoS ALPS2019*, 034 (2020).
- [51] Y.-F. Cai and D. A. Easson, *Asymptotically safe gravity as a scalar-tensor theory and its cosmological implications*, *Phys. Rev. D* **84**, 103502 (2011).
- [52] J. Berges, N. Tetradis, and C. Wetterich, *Non-perturbative renormalization flow in quantum field theory and statistical physics*, *Phys. Rept.* **363**, 223 (2002).
- [53] J. Polonyi, *Lectures on the functional renormalization group method*, *Open Phys.* **1**, 1 (2003).
- [54] J. M. Pawłowski, *Aspects of the functional renormalisation group*, *Annals Phys.* **322**, 2831 (2007).
- [55] J. Berges, N. Tetradis, and C. Wetterich, *Non-perturbative renormalization flow in quantum field theory and statistical physics*, *Phys. Rept.* **363**, 223 (2002).
- [56] M. Reuter, *Nonperturbative evolution equation for quantum gravity*, *Phys. Rev. D* **57**, 971 (1998).
- [57] A. Bonanno, G. Kofinas, and V. Zarikas, *Effective field equations and scale-dependent couplings in gravity*, *Phys. Rev. D* **103**, 104025 (2021).
- [58] A. Bonanno, K. F. Dialektopoulos, and V. Zarikas, *Renormalization group-improved gravitational action: A Lagrangian framework*, *Phys. Rev. D* **112**, 064069 (2025).
- [59] R. A. Konoplya and O. S. Stashko, *Transition from Regular Black Holes to Wormholes in Covariant Effective Quantum Gravity: Scattering, Quasinormal Modes, and Hawking Radiation*, [arXiv:2502.05689](https://arxiv.org/abs/2502.05689).
- [60] G. Guo et al., *Quasinormal modes of black holes with multiple photon spheres*, *JHEP* **2022**, 60 (2022).
- [61] R. J. Borah and U. D. Goswami, *Black hole quasi-periodic oscillations in the presence of Gauss-Bonnet trace anomaly*, *Phys. Lett. B* **872**, 140124 (2026).
- [62] J. Chen and J. Yang, *Shadows and optical appearance of quantum-corrected black holes illuminated by static thin accretions*, *Eur. Phys. J. C* **85**, 512 (2025).
- [63] Y. S. Myung, *Lifshitz black holes in the Hořava-Lifshitz gravity*, *Phys. Lett. B* **690**, 534–540 (2010).
- [64] B. Hazarika and P. Phukon, *Probing Black Hole Phase Transitions through Quasi-Periodic Oscillations* (2025).
- [65] M. B. Awal, B. Hazarika, and P. Phukon, *Quasi-Periodic Oscillations and Parameter Constraints in ModMax Black Holes* (2025).
- [66] J. M. Maldacena, *The Large N limit of superconformal field theories and supergravity*, *Adv. Theor. Math. Phys.* **2**, 231 (1998).
- [67] D. T. Son and A. O. Starinets, *Minkowski space correlators in AdS/CFT correspondence: Recipe and applications*, *JHEP* **9**, 042 (2002).
- [68] D. J. Gogoi and U. D. Goswami, *Quasinormal modes of black holes with non-linear-electrodynamic sources in Rastall gravity*, *Phys. Dark Univ.* **33**, 100860 (2021).
- [69] R. J. Borah and U. D. Goswami, *Quasinormal modes and shadows of black holes in infinite derivative theory of gravity*, *Eur. Phys. J. C* **85**, 940 (2025).
- [70] D. J. Gogoi and U. D. Goswami, *Quasinormal modes and Hawking radiation sparsity of GUP corrected black holes in bumblebee gravity with topological defects*, *JCAP* **06**, 029 (2022).
- [71] F. Hosseinifar et al., *Quasinormal Modes and Topological Characteristics of a Schwarzschild Black Hole Surrounded by the Dehnen Type Dark Matter Halo*, [arXiv:2503.03260 \[gr-qc\]](https://arxiv.org/abs/2503.03260) (2025).
- [72] D. J. Gogoi, R. Karmakar, and U. D. Goswami, *Quasinormal modes of nonlinearly charged black holes surrounded by a cloud of strings in Rastall gravity*, *Int. J. Geom. Meth. Mod. Phys.* **20**, 2350007 (2023).
- [73] R. Karmakar and U. D. Goswami, *Quasinormal modes, temperatures and greybody factors of black holes in a generalized Rastall gravity theory*, *Phys. Scripta* **99**, 055003 (2024).
- [74] G. Mohan, R. Karmakar, R. J. Borah and U. D. Goswami, *Strong Lensing Effect and Quasinormal Modes of Oscillations of Black Holes in $f(R, T)$ Gravity Theory*, *Phys. Dark Univ.* **49**, 102007 (2025).
- [75] R. A. Konoplya and A. Zhidenko, *Quasinormal modes of black holes: From astrophysics to string theory*, *Rev. Mod. Phys.* **83**, 793 (2011).
- [76] G. Franciolini et al., *Effective Field Theory of Black Hole Quasinormal Modes in Scalar-Tensor Theories*, *JHEP* **2**, 127 (2019).
- [77] F. S. Miguel, *EFT corrections to scalar and vector quasinormal modes of rapidly rotating black holes*, *Phys. Rev. D* **109**, 104016 (2024).
- [78] A. Ishibashi, N. Ohta, and D. Yamaguchi, *Quantum improved charged black holes*, *Phys. Rev. D* **104**, 066016 (2021).
- [79] J. M. Pawłowski and D. Stock, *Quantum-improved Schwarzschild-(A)dS and Kerr-(A)dS spacetimes*, *Phys. Rev. D* **98**, 106008 (2018).
- [80] R. A. Konoplya, *Quasinormal modes in higher-derivative gravity: Testing the black hole parametrization and sensitivity of overtones*, *Phys. Rev. D* **107**, 064039 (2023).
- [81] L. de Lima and D. C. Rodrigues, *Schwarzschild–de Sitter spacetime in regular coordinates with cosmological time*, *Phys. Rev. D* **112**, 084062 (2025).
- [82] J. Podolsky, *The structure of the extreme Schwarzschild–de Sitter space-time*, *Gen. Rel. Grav.* **31**, 1703 (1999).
- [83] F.-L. Lin and C. Soo, *Black hole in de Sitter space*, in *Proc. 6th International Symposium on Particles, Strings and Cosmology*, 89 (1998).
- [84] E. Berti, V. Cardoso, and A. O. Starinets, *Quasinormal modes of black holes and black branes*, *Class. Quant. Grav.* **26**, 163001 (2009).
- [85] R. A. Konoplya and A. Zhidenko, *Quasinormal modes of black holes: From astrophysics to string theory*, *Rev. Mod. Phys.* **83**, 793–836 (2011).
- [86] S. H. Völkel, *Quasinormal modes from bound states: The numerical approach*, *Phys. Rev. D* **106**, 124009 (2022).
- [87] K. D. Kokkotas and B. G. Schmidt, *Quasi-Normal Modes of Stars and Black Holes*, *Living Rev. Relativ.* **2**, 2 (1999).
- [88] H.-P. Nollert, *Quasinormal modes: the characteristic ‘sound’ of black holes and neutron stars*, *Class. Quant. Grav.* **16**, R159 (1999).
- [89] D. J. Gogoi and U. D. Goswami, *Quasinormal Modes and Hawking Radiation Sparsity of GUP corrected Black Holes in Bumblebee Gravity with Topological Defects*, *J. Cosmol. Astropart. Phys.* **2022**, 29 (2022).
- [90] C. Gundlach, R. H. Price, and J. Pullin, *Late-time behaviour of stellar collapse and explosions. II. Nonlinear evolution*, *Phys. Rev. D* **49**, 890 (1994).

- [91] Y. Hua and T. K. Sarkar, *Matrix pencil method for estimating parameters of exponentially damped/undamped sinusoids in noise*, IEEE Trans. Acoust. Speech Signal Process. **38**, 814 (1990).
- [92] T. K. Sarkar and O. Pereira, *Using the matrix pencil method to estimate the parameters of a sum of complex exponentials*, IEEE Trans. Antennas Propag. **37**, 48 (1995).
- [93] E. Berti et al., *Mining information from binary black hole mergers: A comparison of estimation methods for complex exponentials in noise*, [Phys. Rev. D **75**, 124017 \(2007\)](#).